An Optimized Reactive Power Compensation Strategy to Extend the Working Range of CHB Multilevel Grid-Tied Inverters

Jinyu Li, *Graduate Student Member, IEEE*, Jie Chen, *Member, IEEE*, and Chunying Gong, *Member, IEEE*

***Abstract*—In the cascaded H-bridge photovoltaic (PV) grid-connected inverter system, the power of PV panels may be unbalanced due to partial shading, aging, dust accumulation, temperature difference, and other reasons. The existing control methods have problems, such as weakened PV energy harvesting ability and the requirement of expanding the working range when the imbalance is severe. This article proposes an optimized reactive power compensation strategy (ORPCS) that first extends the operating range of the system to the maximum under unity power factor. Then, when the system exceeds the upper limit of unity power factor operation under severe imbalance, not only can the maximum PV output energy be harvested with the least amount of reactive power but also the PV voltage fluctuation is small with high-quality grid-connected current when ORPCS is adopted. Last but not least, under balance or mild imbalance yet maintain the advantages of the conventional carrier phase-shift SPWM methods. Simulation and experimental results demonstrate the effectiveness of the proposed method.**

***Index Terms*—Cascaded H-bridge (CHB), improved working performance, minimum reactive power injection, power imbalance.**

Nomenclature

N	Number of H-bridges.
Δu	DC voltage ripple of the H-bridge (HB) with highest power.
v_{ML}	Multilevel output voltage of CHB.
$V_{\mathrm{HB}i}$	Peak fundamental voltage of the ith HB.
v_{g}	Grid voltage.
V_{g}	Peak value of the grid voltage.
i_{g}	Grid current.
i_{gD}	Signal delaying i_{g} by $\pi/2$.
I_{g}	Peak value of the grid current.
I_{gq}	Peak value of the reactive component of the grid current.
I_{gd}	Peak value of the active component of the grid current.
$V_{\mathrm{DC}i}$	DC voltage of the ith HB.
$I_{\mathrm{PV}i}$	DC-side input current of the ith HB.
S	Common modulation index (MI).
ΔS_i	Modification of MI of the ith HB.
S_i	MI of the ith HB.
S_i'	MI of the ith HB with a maximum value of 1.27.
θ_{ig}^*	Reference angle of grid current.
$v_{\mathrm{m}i}$	Reference modulation signal of the ith HB.
$v_{\mathrm{m}i}{}^*$	Modified reference modulation signal of the ith HB.

Manuscript received 5 April 2022; revised 21 July 2022 and 2 December 2022; accepted 21 December 2022. Date of publication 3 January 2023; date of current version 14 February 2023. This work was supported by the Postgraduate Research and Practice Innovation Program of Jiangsu Province (No. KYCX18_0286). Recommended for publication by Associate Editor M. S. ElMoursi. *(Corresponding author: Jie Chen.)*

The authors are with the Center for More Electric Aircraft Power System, Department of Electrical Engineering, College of Automation Engineering, Nanjing University of Aeronautics and Astronautics, Nanjing 211106, China (e-mail: lijinyu@nuaa.edu.cn; chen_jie@nuaa.edu.cn; zjnjgcy@nuaa.edu.cn).

Color versions of one or more figures in this article are available at https://doi.org/10.1109/TPEL.2022.3233896.

Digital Object Identifier 10.1109/TPEL.2022.3233896

I. Introduction

As THE environmental pollution caused by the use of fossil energy, such as petroleum and coal, has threatened the living environment of human beings, carbon neutrality is the general consensus of various countries at present, and it is a development trend to gradually replace the fossil energy with clean energy, such as wind and solar energy. Among the converters adopted in photovoltaic (PV) power generation, the multilevel structure can improve the power quality of grid-connected current and reduce electromagnetic noise [1], [2]. Compared with diode-clamped and flying-capacitor multilevel converters, the cascaded H-bridge (CHB) converter uses the least switching devices when the number of levels increases and has the advantages of modularity, easy maintenance, high efficiency, and high flexibility [3], [4], [5], [6], [7].

The dc sides of the cascaded H-bridge (HB) multilevel grid-connected PV inverter can be connected to PV panels, which can realize the independent maximum power point tracking (MPPT) and has the advantage of improving efficiency [8], [9], [10]. In addition, the CHB PV inverters allow for module-level monitoring and module-level shutdown in case of emergency.

Due to partial shading, dust accumulation, temperature difference, or damage of some PV modules, the power generated between different modules is inconsistent, which may cause the reduction of PV energy harvesting and even system oscillation, resulting harm to the system. Zhao et al. [11], [12], [13] derived the safe working range of the CHB system. When the system exceeds the safe operating range, Iman-Eini et al. [14] proposed to increase the reference dc voltage if the modulation index (MI) of a certain HB cell exceeds 1, allowing this cell to return to the linear modulation region. However, increasing the reference voltage makes the dc-side PV panels deviate from the maximum power point (MPP), leading to a reduction of PV energy.

Aiming at this problem, the third harmonic compensation strategy (THCS) proposed in [15] can make a high-power HB cell work in the linear modulation region without deviating from MPP. The principle of the THCS is to increase the linear modulation region of the system to 1.155 by injecting the positive third harmonic in the high-power cells and injecting the corresponding amount of negative third harmonic into the low power cells. However, when the MI is greater than 1.155, THCS will also be out of safe working range. In response to this problem, the hybrid modulation method [16], [17], [18] uses a strategy of combining low-frequency square wave modulation and high-frequency pulsewidth modulation (PWM) to extend the linear modulation region to 1.27, which solves the problem encountered by the THCS. The hybrid modulation method selects low-frequency square wave signal with certain duty cycle or the high-frequency PWM to control a corresponding HB cell at a certain time interval according to the PV output voltage. However, this method causes irregular fluctuation of PV output voltages [19], [20], [21]. To solve this problem, the harmonic compensation strategy (HCS) [19], [20], [21] not only has a linear modulation region of 1.27 but also uses proportional–integration (PI) algorithm to make the capacitor voltage accurately track the MPP command voltage, thus solving the problem encountered with the hybrid modulation method. The basic principle of HCS is to inject multiple harmonics into the cells with MIs greater than 1 and compensate the same amount of opposite harmonics into the rest cells so that the total amount of positive and negative multiple harmonics cancel out each other. The multiple harmonics in a high MI cell extend the fundamental component of modulation signal, making it peak at 1.27. The phase of modulation signal of HCS is the same as the angle output from the inner loop, which is the phase of the multilevel voltage of the CHB PV inverter. Therefore, the operating range is not extended to the maximum because the ac voltage and ac current of the highest power HB cell is not in the same phase at the upper operating boundary. When the MI of a certain cell is higher than 1.27, the HCS will not be able to output all the energy of the PV panels [21], resulting in a loss of PV energy. The reactive power compensation strategy (RPCS) [22], [23], [24], [25] injects a certain amount of reactive power into the system, which can pull the high-power cells working in the nonlinear modulation region back to the linear modulation region. Thereby, the purpose of expanding the working range of the CHB multilevel PV inverter and harvesting more PV energy is realized. However, compared with RPCS, HCS does not require reactive power injection and can maintain unity power factor (PF) operation in the range of MI greater than 1 and less than 1.27, so RPCS is not optimal to extend the safe working range of CHB PV inverter. Therefore, this leads to the idea of combining HCS and RPCS to achieve better control objectives: First, when the MI is less than 1.27, use HCS to achieve unity PF operation and harvest all PV energies. Second, when the output power imbalance of the PV panels exceeds the upper working boundary of the HCS, adopt the HCS and RPCS (HCS–RPCS) simultaneously to harvest all PV energies.

However, HCS–RPCS is not an optimal idea, which is explained as follows. Although the fundamental amplitude of an HB cell with the highest active power remains at 1.27 (the highest MI that HCS can achieve) when the MI reaches the upper limit of HCS and then the system is injected with reactive power, the fundamental component of this cell is not in phase with its ac-side current. Moreover, because of the injected reactive power, the phase difference between current and voltage on the ac side of the highest MI cell become larger, and the active power of this cell has not reached the maximum state under the amount of reactive power injected. We should extend the active power handling range instead of injecting more reactive power to grid to harvest PV energy. The reactive power required in HCS—RPCS is relative high, so it is not an optimal idea.

This article proposes an optimized HCS-based RPCS (ORPCS), which aims to achieve the goals as follows.

1) When the system reaches the upper boundary of unity PF operation, the fundamental component of modulation signal of the highest power cell reaches the maximum value 1.27 and is in the same phase as its ac-side current, resulting this cell output the maximum active power, so the operating ability to handling imbalance is extended to the upper limit of unity PF operation, ensuring that the PF is the highest when there is no need to inject reactive power.
2) When the system exceeds the upper limit of unity PF operation, this article proposes the minimum reactive power injection control strategy. In this operating state, the fundamental amplitude of the HB cell with the highest active power always maintains 1.27 and is always in phase with its ac-side current so that this HB cell can output the maximum active power under that injected amount of reactive power, and the system can harvest PV energy with the least reactive power. In addition to the above two advantages, other advantages also include.
   a) The injected reactive power is the least, so it can reduce the risk of overcurrent.
   b) Under severe imbalance conditions, the method proposed in this article can harvest more PV energy compared with other methods, such as HCS, RPCS, and THCS.
   c) The dc voltage fluctuation is small, which is also conducive to energy harvesting.

As for leakage current, Zhou et al. [26], [27], [28] analyze and solve the problem of interarray leakage current. In addition, Zhou and Li [26] also analyze and solve the problem of common-mode current between PV panels and ground. These leakage current suppression solutions discussed in [26], [27], and [28] combined with the ORPCS proposed in this article can enhance the performance of the CHB PV system so that the PV system can not only meet the leakage current suppression requirements but also improve the PV energy harvesting capacity.

The rest of this article is organized as follows. Section II introduces the system configuration and operating limitation of the CHB PV system. Section III deduces the realization principle and method of ORPCS. Sections IV and V present the simulation and experimental results, respectively. Finally, Section VI concludes this article.

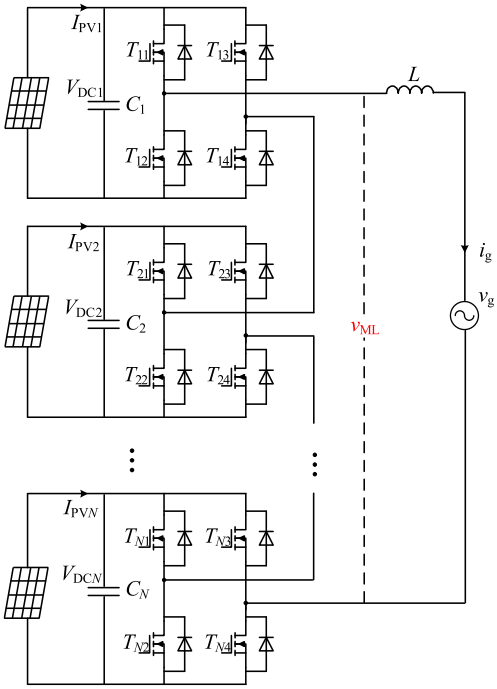

Fig. 1. System configuration.

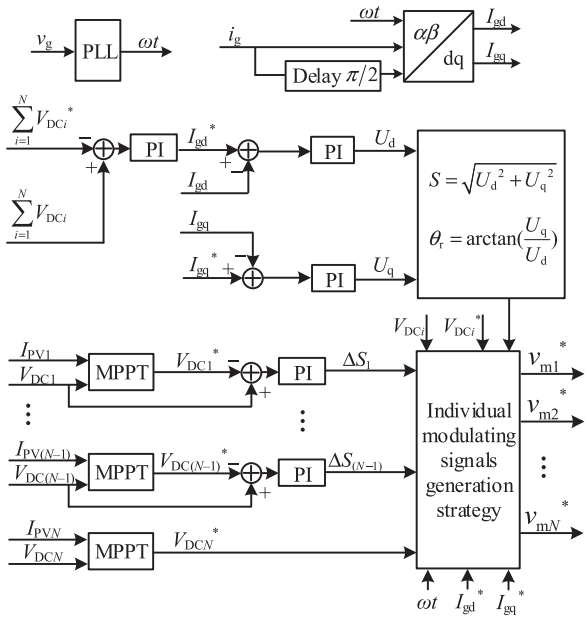

Fig. 2. Control block diagram.

II. System Configuration and Operating Limitation

Fig. 1 shows the main circuit based on the CHB topology. The ac sides of N H-bridge cells are connected in series to obtain the multilevel voltage v_{ML}. The energy is sent to the grid v_{g} through inductor L with the grid-connected current i_{g}. $I_{\mathrm{PV}i}$ is the input current of the ith HB cell. C_i and $V_{\mathrm{DC}i}$ are the dc-side capacitance of the ith cell and its voltage. The dc side of each H-bridge can be connected to several PV modules in series and parallel so as to achieve the purpose of reducing switching devices and cable pairs.

When the powers generated by PV panels are unbalanced, Zhao et al. [11], [12], [13] give the safe operating range of the CHB as follows:

$$I_{\mathrm{PV}i} \le 0.5 I_{\mathrm{g}} \tag{1}$$

where I_{g} represents the amplitude of the grid-connected current. If $I_{\mathrm{PV}i} > 0.5 I_{\mathrm{g}}$, it is beyond the working range of the system. At this time, the grid-connected current needs to satisfy $I_{\mathrm{g}} \ge 2\max(I_{\mathrm{PV}i})$ to maintain the system in linear modulation region according to (1). Therefore, the reactive power injection method proposed in [22], [23], [24], and [25] realizes the return of the high-power cells to the linear modulation region by injecting reactive power into the system. The amount of reactive current injected is

$$I_{\mathrm{gq}} = \sqrt{\left\{\sqrt{2}\max(I_{\mathrm{PV}i})\right\}^2 - (I_{\mathrm{gd}})^2} \tag{2}$$

where I_{gd} and I_{gq} denote the amplitude of active and reactive component of the grid-connected current.

However, for the HCS proposed in [19], [20], and [21], it not only does require reactive power injection (the amount of reactive power injected is 0) but also uses the PI controllers to accurately track the MPP voltage of the PV panels when $1 < \mathrm{MI} \le 1.27$ so that all PV energies can be harvested. The output current of the PV panels under HCS control should satisfy

$$I_{\mathrm{PV}i} \le \frac{1.27}{2} I_{\mathrm{g}}. \tag{3}$$

However, when $I_{\mathrm{PV}i} > 1.27 I_{\mathrm{g}} / 2$, HCS cannot achieve the cell with MI exceeding 1.27 to work at the MPP, which will lead to energy loss [21].

However, the PV energy loss can be prevented by injecting a certain amount of reactive power into the system when $I_{\mathrm{PV}i} > 1.27 I_{\mathrm{g}} / 2$ under HCS control. But HCS–RPCS is not an optimal strategy as explained. In a severe imbalance case such that it exceeds the upper working boundary of HCS and then the system is injected with reactive power, although the fundamental amplitude of the cell with the highest active power remains at 1.27 (the highest MI that HCS can achieve), the fundamental component of this cell is not in phase with the ac-side current, so the active power of this cell has not reached the maximum state under the amount of the injected reactive power, indicating that HCS–RPCS is not optimal. Instead, the idea of this article is to propose an optimized RPCS to achieve the purpose of harvesting energy by expanding the active power handling range rather than injecting more reactive power into the system, that is to say, harvesting more energy with the least reactive power.

III. Optimized RPCS

The basic control block diagram of the CHB grid-tied PV inverter is shown in Fig. 2. The PI regulators in the dq coordinate adjust the dc voltages and grid-connected current to achieve no static error control. The MPPT block outputs the MPP command

voltage $V_{\mathrm{DC}i}{}^*$, the sum of which $\sum_1^N V_{\mathrm{DC}i}^*$ and the sum of the dc voltage feedback signals $\sum_1^N V_{\mathrm{DC}i}$ are adjusted by the outer loop PI regulator to obtain the reference active signal $I_{\mathrm{gd}}{}^*$ of the grid-connected current. The real-time angle ωt obtained by the phase-locked loop, the grid-connected current i_{g}, and the i_{gD} delaying i_{g} by $\pi/2$ are sent to dq transformation to generate the active feedback signal I_{gd} and the reactive feedback signal I_{gq} of the grid-connected current. I_{gd} and I_{gq} are adjusted by the PI regulators in the inner loop, which output the d-axis reference signal U_{d} and q-axis reference signal U_{q}. Then, the average modulation ratio S and angle θ_{r} can be obtained as follows:

$$S = \sqrt{U_{\mathrm{d}}^2 + U_{\mathrm{q}}^2} \tag{4}$$

$$\theta_{\mathrm{r}} = \arctan\left(\frac{U_{\mathrm{q}}}{U_{\mathrm{d}}}\right). \tag{5}$$

And then get the common modulation signal as follows:

$$v_{\mathrm{m}} = S\sin(\omega t + \theta_{\mathrm{r}}). \tag{6}$$

For the control of dc voltage of a cell, the reference signal $V_{\mathrm{DC}i}{}^*$ from the MPPT block and the feedback value $V_{\mathrm{DC}i}$ are automatically adjusted by a PI regulator without static error from which the fine-tuning duty cycle ΔS_i is obtained and superimposed on the base MI of this cell. Therefore, the active power of this cell is modified, enabling the capacitor voltage $V_{\mathrm{DC}i}$ that tracks the reference voltage $V_{\mathrm{DC}i}{}^*$ at MPP.

For the first to the (N–1)th cells, their modification signals of MI are calculated by the PI regulators, which together with the base signal S constitute the MI of this cell as follows:

$$S_i = S + \Delta S_i, \quad i = 1, \ldots, N-1. \tag{7}$$

When the modulating signal of a cell becomes a square wave with amplitude of 1, it can achieve the maximum fundamental amplitude, which is 1.27. That is to say, the actual maximum MI of a cell is 1.27. In order to reflect the actual MI of a cell, the

$$S_i' = \begin{cases} 1.27 & S_i > 1.27 \\ S_i & S_i \le 1.27 \end{cases}, \quad i = 1, \ldots, N-1 \tag{8}$$

is used to participate in the closed-loop control.

According to the principle that the sum of the voltage variations produced by each fine-tuning signals should be zero, the fine-tuning signal of the last cell is calculated as follows:

$$\Delta S_N = -\frac{1}{V_{\mathrm{DC}N}} \sum_{i=1}^{N-1} (S_i' - S) V_{\mathrm{DC}i} \tag{9}$$

and further get the MI of the last cell

$$S_N = S + \Delta S_N. \tag{10}$$

Similarly, limit the maximum value of S_N to 1.27

$$S_N' = \begin{cases} 1.27 & S_N > 1.27 \\ S_N & S_N \le 1.27. \end{cases} \tag{11}$$

$S_i'(i = 1, \ldots, N)$ reflects the MI and the relative amount of power delivered by each cell. When the system is slightly unbalanced, we can use the sinusoidal reference signal PWM to achieve simple control (working mode 1 in Section III-A). When the system is medium unbalanced, we propose a strategy to extend the system to the upper limit of the working range under unity PF using nonsinusoidal reference signal PWM (working mode 2 in Section III-B). The upper working boundary of this working mode is that the fundamental component of the cell transferring the highest active power reaches the maximum (the MI reaches the maximum value of 1.27) and is in the same phase as the ac current. When the imbalance continues to expand, we propose the strategy of harvesting PV energy with the least reactive power (working mode 3 in Section III-C).

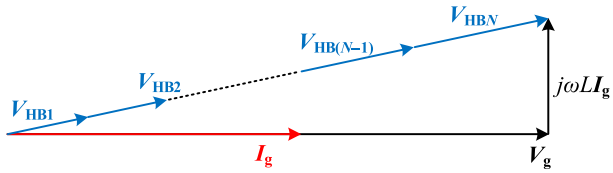

Fig. 3. Phase diagram of mode 1.

A. Working Mode 1 Under Slight Imbalance

When the maximum MI, $\max S_i'(i = 1, \ldots, N)$, is less than 1, there is no overmodulation problem, and the system control can be realized by using the conventional sinusoidal modulation signal. This operation state is defined as "slight imbalance." The upper boundary of this working mode is that the highest MI is less than or equal to one, and the modulation signal of each HB in this mode is given as follows:

$$v_{\mathrm{m}i} = S_i' \sin(x) \tag{12}$$

where

$$x = \omega t + \theta_{\mathrm{r}}. \tag{13}$$

The phase diagram of this working mode is shown in Fig. 3.

When the MI is greater than 1, this will exceed the operating range of mode 1 and will automatically enter mode 2.

B. Working Mode 2 Extending the Operating Range to the Limit Under Unity PF in Medium Imbalance Conditions

When the maximum MI, $\max S_i'(i = 1, \ldots, N)$, is greater than 1, it will exceed the adjustable range of the sinusoidal modulation signal control (mode 1). Therefore, this article will propose a new method to let the system enter the working mode 2 extending the linear modulation region. The goals to be achieved are as follows: First, Mode 1 and mode 2 can be switched seamlessly, and the inverter output current transitions smoothly without overshoot during the switching process. Second, extend the working range of the system to the maximum under the unity PF.

The lower boundary of mode 2 is that the maximum MI, $\max S_i'(i = 1, \ldots, N)$, is equal to 1, as shown in the curve $\sin(x)$ in Fig. 4(a). The upper boundary is the extension of the operating range of the system to the maximum under unity PF (the fundamental component of modulation signal of the highest power cell reaches its maximum value, i.e., 1.27, and in the

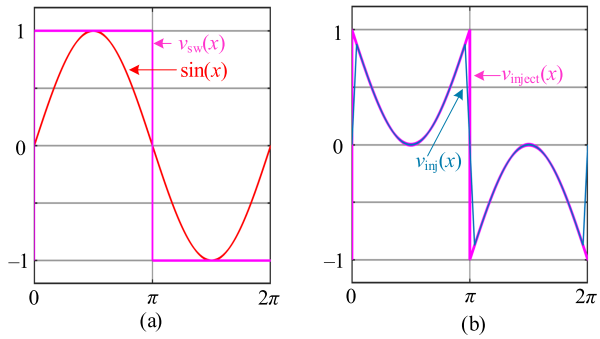

Fig. 4. Operating boundaries of mode 1 and mode 2 and the injected waveform. (a) Operating boundaries of mode 1 and mode 2. (b) Waveform to be injected in mode 2.

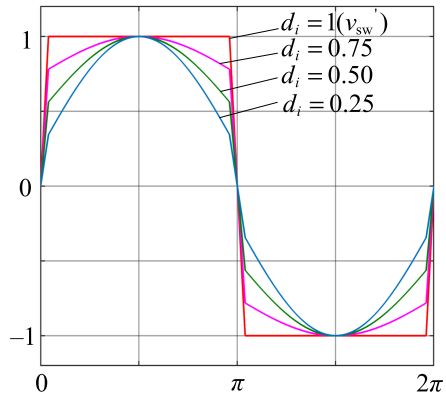

Fig. 5. Modulation waveforms of the overmodulation cells with different d_i.

same phase as the ac-side current). The upper boundary can be expressed as follows:

$$v_{sw}(x) = \begin{cases} 1 & \sin(\omega t + \theta_{ig}^*) \geq 0 \\ -1 & \sin(\omega t + \theta_{ig}^*) < 0 \end{cases} \tag{14}$$

where the reference current angle θ_{ig}^* is given as follows:

$$\theta_{ig}^* = \arctan \frac{I_{gq}^*}{I_{gd}^*}. \tag{15}$$

Equation (14) represents a square wave signal in the same phase as the ac current, and its waveform is $v_{sw}(x)$, as shown in Fig. 4(a). When the system operates between the lower and upper boundaries of mode 2, the solution proposed in this article is as follows. The region between the upper boundary $v_{sw}(x)$ and the lower boundary $\sin(x)$ is the adjustable region of the modulation signal of overmodulation cells in mode 2, and the difference can be expressed as follows:

$$v_{inject}(x) = v_{sw}(x) - \sin(x). \tag{16}$$

When all $v_{inject}(x)$ is injected into $\sin(x)$, the upper boundary $v_{sw}(x)$ can be obtained. When zero times $v_{inject}(x)$ is injected into $\sin(x)$, the lower boundary $\sin(x)$ can be obtained. When the system operates between the upper and the lower boundaries, we inject a part of $v_{inject}(x)$, that is, $d_i v_{inject}(x), d_i \in [0, 1]$, into the unity signal $\sin(x)$ such that the purpose of continuously adjusting the fundamental component of a cell is achieved. When $S_i' = 1$, the injection amount of $v_{inject}(x)$ should be 0, so the injection factor d_i should be equal to 0; when $S_i' = 1.27$, all $v_{inject}(x)$ should be injected, so d_i should be equal to 1. When S_i' increases from 1 to 1.27, d_i should rise from 0 to 1, so set the relationship between S_i' and d_i to

$$d_i = \frac{1}{0.27}(S_i' - 1). \tag{17}$$

Because $v_{inject}(x)$ contains step changes, as shown in Fig. 4(b), they will cause the modulation signal to contain step changes, which will cause the grid-connected current to distort under the carrier phase-shift PWM technique implemented by DSP controller digitally. So, the $v_{inject}(x)$ is replaced by $v_{inj}(x)$, as shown in Fig. 4(b), to eliminate the step changes

$$v_{inj}(x) = v_{sw}'(x) - \sin(x) \tag{18}$$

where

$$v_{sw}'(x) = \begin{cases} 1 & 9\sin(\omega t + \theta_{ig}^*) > 1 \\ 9\sin(\omega t + \theta_{ig}^*) & -1 \leq 9\sin(\omega t + \theta_{ig}^*) \leq 1 \\ -1 & 9\sin(\omega t + \theta_{ig}^*) < -1. \end{cases} \tag{19}$$

For cells with MIs greater than 1, the modulation signals are expressed as follows:

$$v_{mi}(x) = \sin(x) + d_i v_{inj}(x), \quad d_i \in [0, 1]. \tag{20}$$

When the value of d_i varies with different values, the waveforms are shown in Fig. 5.

The sum of the fundamental components produced by S_i' should be equal to the sum of the fundamental components produced by the common modulation index S (without independent MPPT control loop activated) to reduce the coupling effects between the independent MPPT control loop and the inner current control loop [29]

$$\sum_{i=1}^{N} [S_i' \sin(x) V_{DCi}] = \sum_{i=1}^{N} [S \sin(x) V_{DCi}]. \tag{21}$$

The sum of the instantaneous output voltages on the ac side of CHB produced by the modulation signal $v_{mi}(x)$ of each cell should be equal to the sum of the instantaneous voltages produced by the common modulation signal $S\sin(x)$ [29]

$$\sum_{i=1}^{N} [v_{mi}(x) V_{DCi}] = \sum_{i=1}^{N} [S \sin(x) V_{DCi}]. \tag{22}$$

Subtracting (21) from (22) to obtain the instantaneous voltage balance formula

$$\sum_{i=1}^{N} \{[v_{mi}(x) - S_i' \sin(x)] V_{DCi}\} = 0. \tag{23}$$

Assuming that the number of cells with MIs no greater than 1 is k, the MIs of the remaining (N–k) cells are greater than 1.

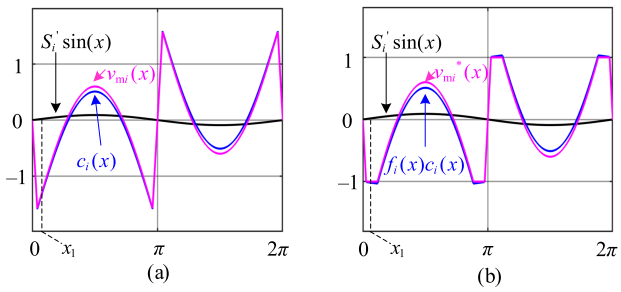

Fig. 6. Overmodulation phenomenon near zero-crossing point. (a) Modulation waveform before correction. (b) Modulation waveform after correction.

From (23), it can be deduced that

$$\sum_{i=1}^{k}\{[v_{mi}(x)-S_i'\sin(x)]V_{DCi}\} = \sum_{i=k+1}^{N}\{[S_i'\sin(x)-v_{mi}(x)]V_{DCi}\}. \quad (24)$$

Since the modulating signals of the cells with MIs greater than 1 are already given by (20), the right-hand term of (24) can be calculated as $c(x)$ within one execution cycle of the controller

$$c(x)=\sum_{i=k+1}^{N}\{[S_i'\sin(x)-v_{mi}(x)]V_{DCi}\}. \quad (25)$$

In order for the balance formula (23) to hold in any case, the $c(x)$ can be distributed to the modulating signal $S_i'\sin(x)$ of the 1–k cells whose MIs are no greater than 1, and let $\sum_1^k\{[v_{mi}(x)-S_i'\sin(x)]V_{DCi}\}$ be equal to $c(x)$.

For a cell whose S_i' is less than 1, the smaller S_i' is, the more $c(x)$ we can distribute to this cell. Its modulating signal is expressed as follows:

$$\begin{aligned} v_{mi}(x) &= S_i'\sin(x) \\ &\quad + \frac{(1-S_i')V_{DCi}}{(1-S_1')V_{DC1}+\cdots+(1-S_k')V_{DCk}}c(x)\frac{1}{V_{DCi}} \\ &= S_i'\sin(x)+\underbrace{\frac{(1-S_i')c(x)}{(1-S_1')V_{DC1}+\cdots+(1-S_k')V_{DCk}}}_{c_i(x)}. \end{aligned} \quad (26)$$

Equation (26) shows that the modulating signals of the first to the kth cells consist of the components $S_i'\sin(x)$ and $c_i(x)$. Similarly, for the modulating signals of the $(N–k+1)$th to the Nth cells, in addition to the fundamental components $S_i'\sin(x)$, the corresponding components $c_i(x)$ can also be extracted as follows:

$$c_i(x)=v_{mi}(x)-S_i'\sin(x). \quad (27)$$

The modulating signals of the 1–k cells are superimposed with $c_i(x)$. However, when the absolute value of $c_i(x)$ added to a cell is too large, the modulating waveform of this cell will be overmodulated near the current zero-crossing point. This phenomenon is shown at point x_1 in Fig. 6(a). If the instantaneous value of $c_i(x)$ at point x_1 is less than $-(S_i'\sin(x)+1)$, it will inevitably cause the modulation signal $v_{mi}(x)$ to be less than -1, resulting in overmodulation phenomenon; in fact, the instantaneous value of $c_i(x)$ at point x_1 is less than $-(S_i'\sin(x)+1)$. If $c_i(x)$ is multiplied by a factor of $-(S_i'\sin(x)+1)/c_i(x)$ and then superimposed on $S_i'\sin(x)$, the modulating signal $v_{mi}(x)$ of this cell can be made exactly equal to –1, thus avoiding overmodulation problem at point x_1. This factor can be expressed as follows:

$$f_i(x)=\begin{cases} -(S_i'\sin(x)+1)/c_i(x) & v_{mi}(x)<-1 \\ 1 & -1\le v_{mi}(x)\le 1 \\ -(S_i'\sin(x)-1)/c_i(x) & v_{mi}(x)>1. \end{cases} \quad (28)$$

However, each cell has different factor $f_i(x)$, which in turn makes the instantaneous voltage balance formula (23) not satisfied. If the left- and right-hand sides of (23) are both multiplied by a common factor, it is found that (23) holds; that is to say, if the components $c_i(x)$ of the 1–N cells are multiplied by a common factor, (23) can still be satisfied. Therefore, we take the minimum value among $f_i(x)$ as this common factor

$$f(x)=\min_{i=1}^{k} f_i(x) \quad (29)$$

which enable that the modulation signal of each cell is distributed between –1 and 1, thereby solving the problem of overmodulation near the zero-crossing points of the current caused by the components $c_i(x)$ injected.

Consequently, the new modulating signals are modified as $v_{mi}^*(x)$

$$v_{mi}^*(x)=S_i'\sin(x)+f(x)c_i(x). \quad (30)$$

C. Working Mode 3 for Harvesting PV Energies With Minimum Reactive Power

When the imbalance of PV energies exceeds the operating range of working mode 2, the output voltages of the PV panels with higher power will not be tracked at the MPP if no additional measures are taken at this time, which will lead to the loss of PV energies. However, injecting reactive power can solve this problem [22], [23], [24], [25].

The control goals of mode 3 are that to realize each cell work at MPP with the least reactive power so as to fully harvest the PV energies.

At the upper boundary of mode 2, the MI of the cell with the highest power is 1.27 (theoretical maximum value), and its fundamental component is in the same phase as its ac-side current, thus reaching the upper boundary of zero-reactive-power-injection operation (unity PF operation case). When the unbalanced power exceeds the upper limit of mode 2, reactive power injection is required to harvest all energies from each panel, thus entering working mode 3. In order to achieve the least amount of reactive power injected, it is necessary to keep the following points in mind.

1) The MI of the highest power cell is always equal to 1.27.
2) The fundamental component of the highest power cell is in the same phase as its ac-side current.

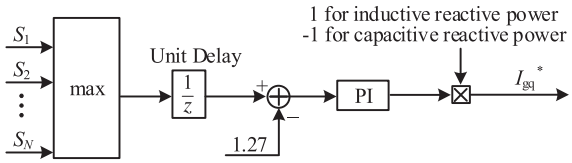

Fig. 7. Minimum reactive current reference signal generation method.

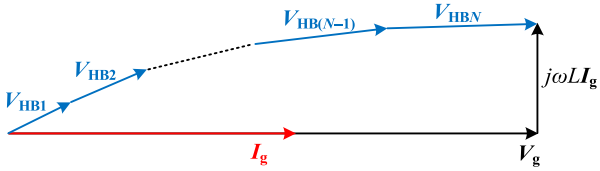

Fig. 8. Phase diagram of mode 2.

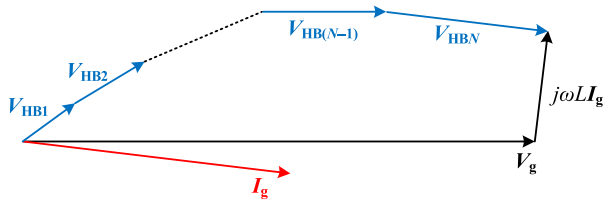

Fig. 9. Phase diagram of mode 3.

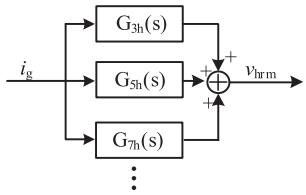

Fig. 10. Resonant control signal.

When the MI of the highest power cell is maintained at 1.27, it can be seen from (20) proposed in this article that the corresponding fundamental component of the modulating signal is 1.27 and is in phase with the ac current, which is an automatic process. Therefore, working mode 3 only need to achieve the following points.

1) When the system has to inject reactive power to harvest all PV energies, how to make the MI of the highest power cell exactly 1.27 in order to keep the minimum reactive power injection.
2) When the system returns to mode 2, the reference reactive current signal should automatically become zero.

In order to achieve these two goals, the control principle proposed in this article is shown in Fig. 7.

The working principle of Fig. 7 is explained as follows. When the system works in mode 2, maxS_i is less than 1.27 so that the reference reactive current $I_{\rm gq}{}^*$ is automatically reduced to 0, the lower saturation limit of the PI (the PI antisaturation method is clamping). When the system enters mode 3 from mode 2, the input error signal of the PI regulator is positive, and the PI output increases, which will automatically track maxS_i to 1.27 and stabilize it at 1.27, thereby achieving the least reactive power control.

When the PCC voltage is lower than the rated value, the output of the PI regulator in Fig. 7 should be multiplied by –1 to assist the low-voltage ride through function. When the PCC voltage is higher than the rated value, the output of PI is multiplied by 1 to assist the grid to stabilize the PCC voltage at the rated value.

The reason why the input signal in Fig. 7 uses S_i instead of S_i' is that S_i' has been limited to 1.27 and below. However, S_i can make the input signal of the PI regulator in Fig. 7 positive, realizing the positive increase of the output of the PI regulator.

The phase diagrams of mode 2 and mode 3 are shown in Figs. 8 and 9. Comparing the phase diagrams of mode 1, mode 2, and mode 3, it can be seen that mode 1 and mode 2 always work at unity PF. It can be seen from the phase diagram of mode 3 that the output voltage $\boldsymbol{V}_{\mathbf{HB}N}$ and the current $\boldsymbol{I}_{\mathbf{g}}$ of the HB whose MI exceeds 1.27 (take HB$_N$ as an example) are in the same phase, which make this high-power HB transmit pure active power from PV panels.

The reactive power can be processed according to different operation scenarios, which can be divided into four types. In operation scenario 1, there is only one inverter in this scenario and it is not allowed to inject reactive power into the grid. In operation scenario 2, there are more than one inverter in the system. In operation scenario 3, there is a reactive power compensation device in the system. In operation scenario 4, the system allows to inject reactive power.

For the operation scenario 1, we can set the reactive power command $I_{\rm gq}{}^*$ to zero to obtain unity PF operation. For the operation scenario 2, the inverter in future PV system is required to generate reactive power to support the stable operation of utility grid. That is to say, the inverter has reactive power compensation capability. The reactive power of a certain inverter can be absorbed by another inverter. This not only increases the PV energy harvesting capacity under unbalanced input powers with the strategy proposed in this article but also compensates for reactive power. For the operation scenario 3 equipped with a reactive power compensation device, the reactive power under severe imbalance can also be compensated by the reactive power compensation device. For the operation scenario 4, according to the method proposed in this article, the system can realize that each module works in the MPPT state to increase the power generation and can realize the minimum reactive power operation. Because the reactive power is reduced, the rms value of the inverter output current is smaller and it is beneficial to improve the efficiency and energy harvesting capacity.

D. Harmonics Suppression

There are multiple methods to achieve harmonic suppression and improve grid-connected power quality. The resonant controller is an effective method [30]. The resonant control strategy is shown in Fig. 10. The resonant controller can be expressed as follows:

$$G_{ih}(s) = \frac{2K_{ri}\omega_c s}{s^2 + 2\omega_c s + (i\omega_0)^2}, \quad i = 3 \quad 5 \quad 7 \quad \ldots \tag{31}$$

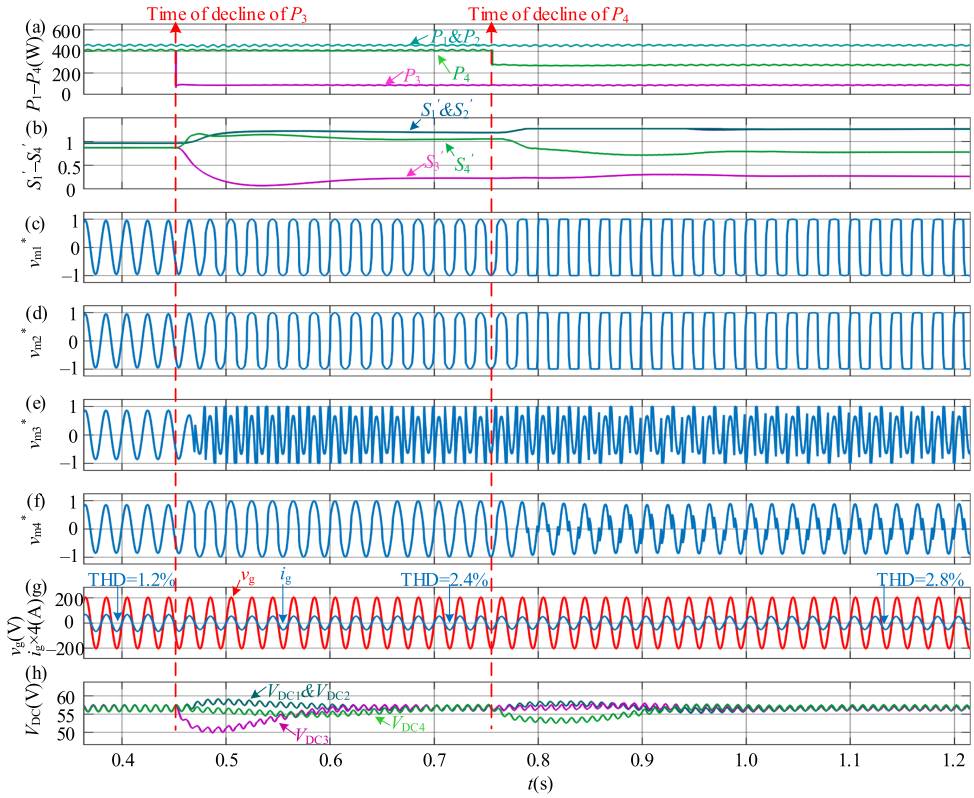

Fig. 11. Simulation waveforms of ORPCS. (a) Power of each cell. (b) MIs. (c) Modulation wave of cell 1. (d) Modulation wave of cell 2. (e) Modulation wave of cell 3. (f) Modulation wave of cell 4. (g) PCC voltage and current. (h) DC voltages.

where ω_0 is the fundamental frequency of the grid voltage v_g and ω_c is the bandwidth of the resonant controller, taken as $\omega_c = 4\pi$ rad/s in this article.

The total output signal v_{hrm} of the resonant controller, as shown in Fig. 10, is superimposed on the modulation signal of each HB, which can achieve the effect of improving the quality of grid-connected power. Since the main goal of this article is how to harvest more energy under unbalanced PV modules, and the mechanism of resonant control strategy has been discussed in detail in [30]; therefore, the resonant control mechanism is not discussed in detail in this article.

E. Novel and Original Contribution of This Article

The HCS in [19], [20], and [21] successfully improves the working range of system and it has several advantages, such as higher MI up to 1.27 and smaller PV voltage fluctuation, which is beneficial for PV energy harvesting. However, HCS cannot achieve full harvesting of PV energy for modules whose MIs are greater than 1.27 [21]. If reactive power is injected in HCS at this time, the amount of reactive power injected is not the least. This article proposes an optimized strategy to achieve minimum reactive power injection while retaining all the advantages of HCS to achieve more energy harvesting in unbalanced conditions, which is the original contribution of this article.

IV. Simulation and Comparison

In order to verify the correctness and effectiveness of the proposed on a four H-bridges cascaded system and compare the control effects with the existing strategies, such as RPCS, THCS, and HCS, to show the advantages and disadvantages of ORPCS in MATLAB/Simulink.

TABLE I
PV Parameters

Symbol	Parameter	Value
P_{max}@25°	Maximum power	250 W
V_{oc}@25°	Open-circuit voltage	37.6 V
I_{sc}@25°	Short-circuit current	8.55 A
V_{MPP}@25°	Voltage at MPP	31 V
I_{MPP}@25°	Current at MPP	8.06 A
P_{max}@45°	Maximum power at 45°	229 W
V_{MPP}@45°	Voltage at MPP at 45°	28.3 V

In simulation, the dc side of each H-bridge is connected to two PV modules (PV_1 and PV_2 are connected in series and then connected to HB_1; PV_3 and PV_4 are connected in series and then connected to HB_2; PV_5 and PV_6 are connected in series and then connected to HB_3; and PV_7 and PV_8 are connected in series and then connected to HB_4). The parameters of each PV are shown in Table I, and the rest of the simulation parameters of the system are shown in Table II.

When the average MI of each cell is high, that is, the sum of each dc voltage is low, the ability to handle unbalanced power becomes weaker. If imbalance occurs at this time, it is more harmful to the system. The temperature of the PV panel is higher

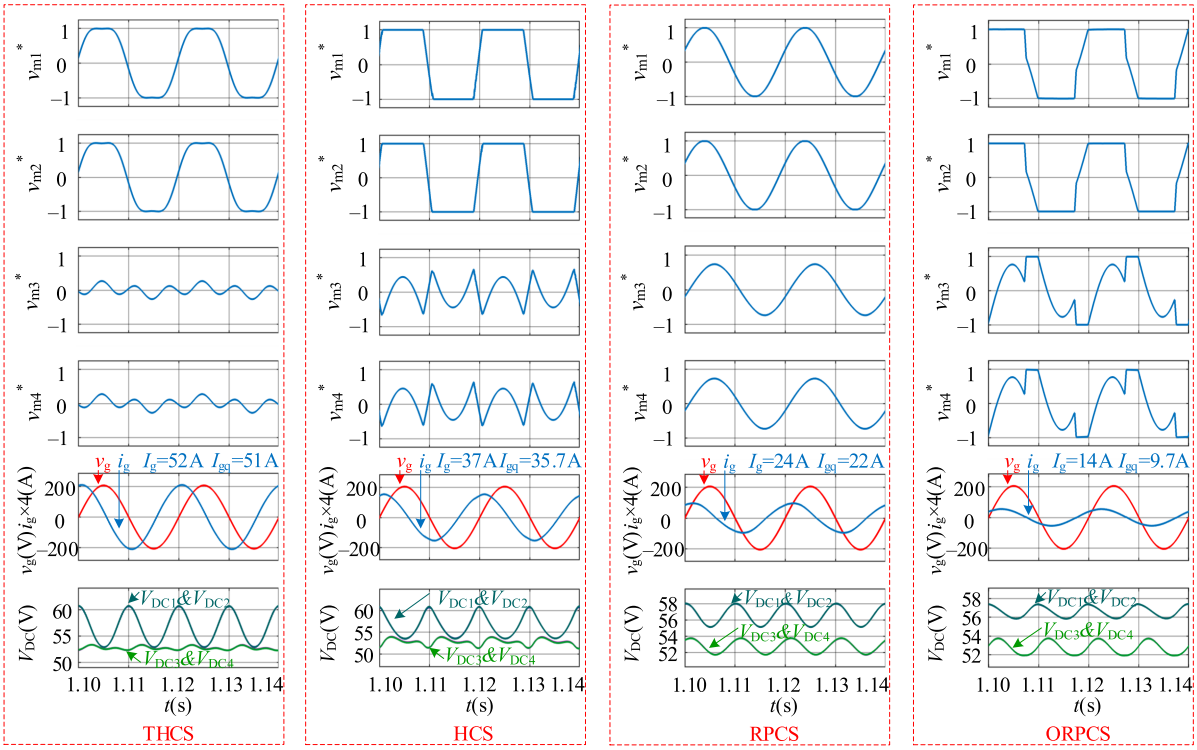

Fig. 12. Comparison of THCS, HCS, RPCS, and ORPCS under severe unbalanced condition. (a) Simulation results of THCS. (b) Simulation results of HCS. (c) Simulation results of RPCS. (d) Simulation results of ORPCS.

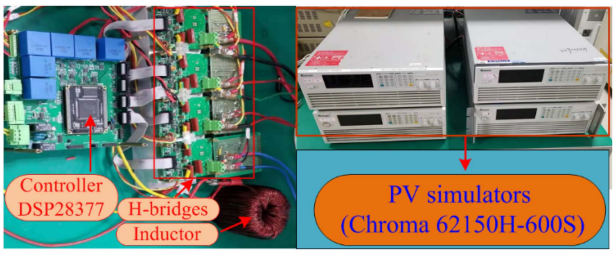

Fig. 13. Experimental platform.

TABLE II
SIMULATION PARAMETERS

Symbol	Parameter	Value
N	Number of H-Bridges	4
L	Filter inductance	4 mH
C	DC-side capacitance	13.6 mF
V_g	Grid voltage amplitude	208 V
f_g	Grid voltage frequency	50 Hz
f_s	Switching frequency	2.5 kHz
T_S	Control system sample time	50 μs
($k_{p,v}$, $k_{i,v}$)	Voltage loop PI coefficients	(0.54, 8.9)
($k_{p,ig}$, $k_{i,ig}$)	Current loop PI coefficients	(0.0074, 0.33)
($k_{p,vb}$, $k_{i,vb}$)	Balancing loop PI coefficients	(0.08, 1.3)
($k_{p,rl}$, $k_{i,rl}$)	Reactive loop PI coefficients	(0.9, 15)
(ΔV_{MPPT}, Δt)	MPPT step (P&O) coefficients	(2 mV, 10 ms)

the total dc voltage is also lower. Therefore, the temperature of the PV panels is set to 45° during the simulation test.

Fig. 11 shows the simulation waveforms of the three modes under the ORPCS control strategy. Before 0.45 s, the system was working in mode 1 in which the irradiation levels of each PV panels are E_1–E_4 = 1000 W/m^2 and E_5–E_8 = 900 W/m^2, and the output powers of HBs are $P_1 = P_2 = 458$ W and $P_3 = P_4 = 412$ W. The MIs of HB_1 and HB_2 are the same and the highest (0.96), the grid-connected current THD is 1.2%, and the ripple of the dc voltage of the highest power HB (HB_1) is $\Delta u = 1.88$ V. When $t = 0.45$ s, the irradiation levels of the panels 5 and 6 are decreased to $E_5 = E_6 = 200$ W/m^2 with $P_3 = 88$ W and the irradiation levels and powers of the other panels remain unchanged. At this time, the system enters mode 2. In this state, the MI of HB_1 is 1.2, $\Delta u = 1.46$ V, and THD = 2.4%. When $t = 0.75$ s, E_7 and E_8 falls to 600 W/m^2, $P_4 = 274$ W, and the light intensities and powers of the other panels remain unchanged, thus entering mode 3. Under this condition, THD = 2.8% and $\Delta u = 1.32$ V. If system do not enter mode 3, not all of the electricity generated by the PV panels will be harvested, resulting in a waste of energy. It can be seen from Fig. 11 that the ORPCS can achieve a smooth transition of the grid-connected current between different modes, and the grid-connected current quality is high in the three modes with a low THD.

Fig. 12 compares the control effects of ORPCS with THCS, HCS, and RPCS under the same conditions. The simulation parameters are: E_1–E_4 = 1000 W/m^2, E_5–E_8 = 100 W/m^2, $P_1 = P_2 = 458$ W, $P_3 = P_4 = 40$ W, and the temperature is 45°. In this working condition, the output power of each panels varies greatly, which is beyond the range of unity PF operation and it is impossible to harvest all the energies of each panel, but the injection of reactive power can solve this problem. Fig. 12(a)

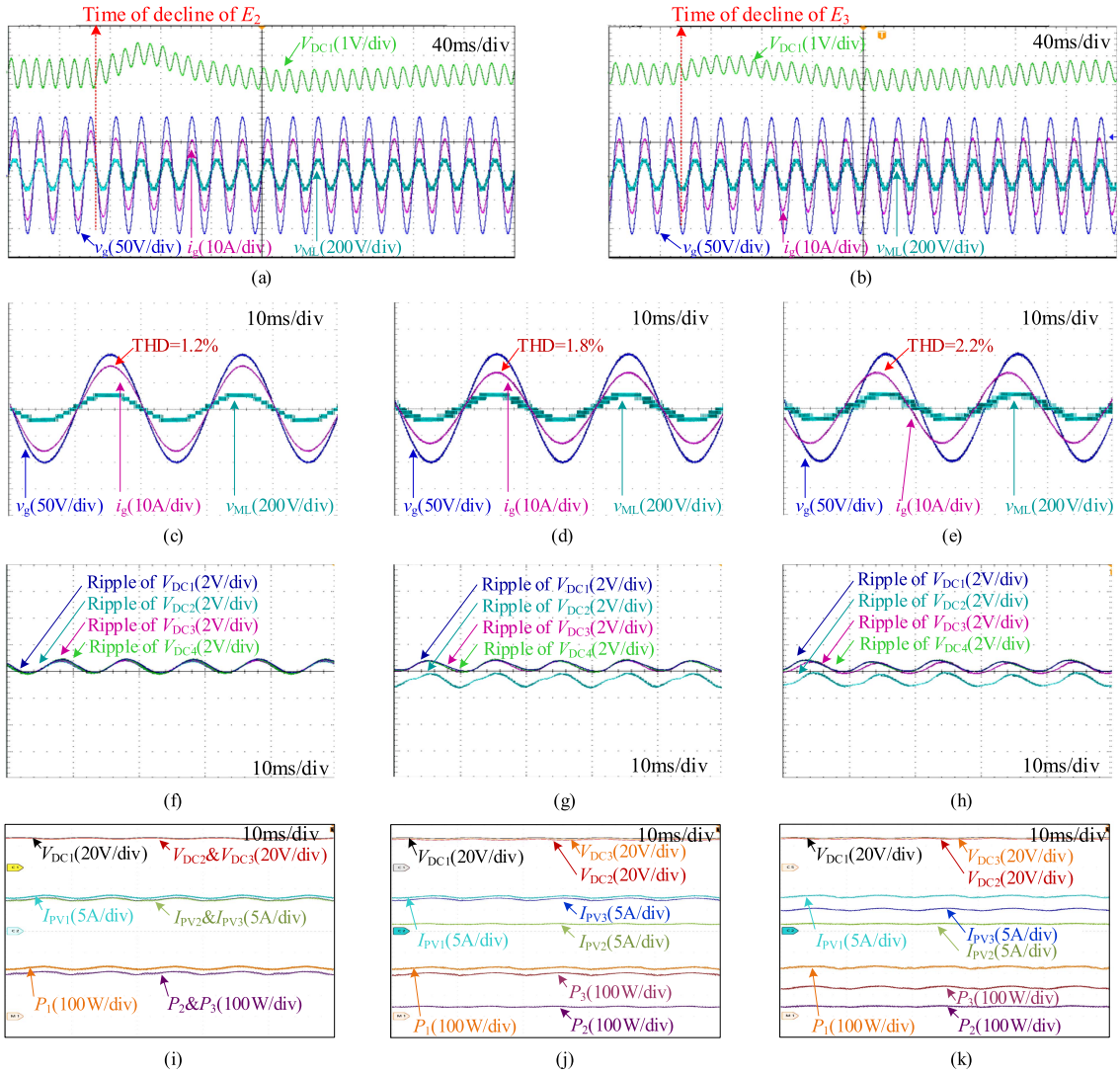

Fig. 14. Transient- and steady-state waveforms when switching between three modes with ORPCS. (a) Switch from mode 1 to mode 2. (b) Switch from mode 2 to mode 3. (c), (f), and (i) Steady-state waveform of mode 1. (d), (g), and (j) Steady-state waveform of mode 2. (e), (h), and (k) Steady-state waveform of mode 3.

shows the waveforms of THCS. The grid-connected current is 52 A peak, and the reactive component of current is 51 A peak, with PF = 0.18. A large amount of reactive current makes the grid-connected current very large, which threat the safe operation of the converter, and a large amount of reactive power leads to a large ripple of the output voltage of high-power PV panel. The dc voltage ripple of HB_1 is $\Delta u = 7.8$ V. When the HCS is adopted, as shown in Fig. 12(b), the injected reactive current is reduced to 35.7 A peak, the grid-connected current becomes 37 A peak, and the PF is increased to 0.27, with $\Delta u = 6.2$ V. When the RPCS is adopted, as shown in Fig. 12(c), the injected reactive current is reduced to 22 A peak, the grid-connected current is reduced to 24 A peak, and the PF is increased to 0.41 with $\Delta u = 2.84$ V. When the ORPCS is adopted, as shown in Fig. 12(d), the injected reactive current is reduced to 9.7 A peak, the PF is improved to 0.72, and $\Delta u = 1.54$ V. It can be seen that the ORPCS not only requires the least amount of reactive power but also has the smallest ripple of dc voltage. Although the four control strategies transmit the same amount of active power, the required reactive power varies greatly.

V. Experiment and Comparison

In this section, the strategy proposed in this article will be verified on an experimental platform and compared with other methods, such as THCS, HCS, and RPCS. The platform, as shown in Fig. 13, consists four H-bridges controlled by DSP28377 and powered by four PV panel simulators (Chroma 62150H-600S). An H-bridge connects a PV simulator. Each PV simulators adopt the parameters, as shown in Table I. In addition, the Infineon IPP060N06N MOSFET is used as the switching devices. The rest of the experimental parameters are shown in Table III.

Fig. 14 shows the transient waveforms and steady-state waveforms of ORPCS. Fig. 14(a) shows the transient waveform of switching from mode 1 to mode 2. The converter first works in mode 1 (irradiation levels and corresponding panel powers are:

TABLE III
EXPERIMENTAL PARAMETERS

Symbol	Parameter	Value
N	Number of H-Bridges	4
L	Filter inductance	2 mH
C	DC-side capacitance	27.2 mF
V_g	Grid voltage amplitude	104 V
f_g	Grid voltage frequency	50 Hz
f_s	Switching frequency	2.5 kHz
T_S	Control system sample time	50 μs

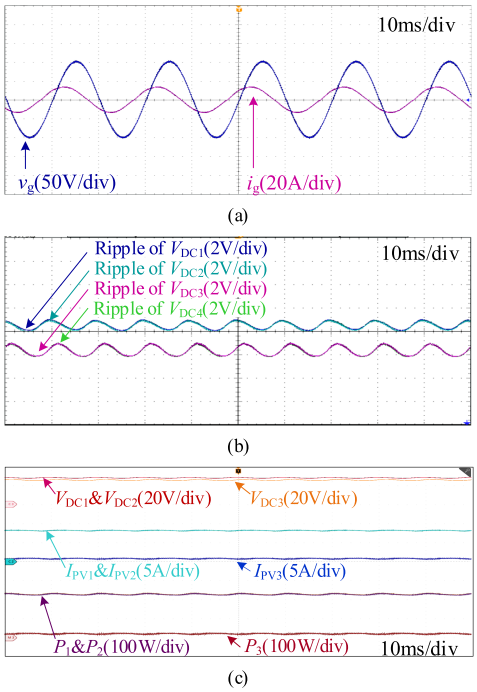

Fig. 15. Experimental waveforms of ORPCS. (a) AC voltage and current. (b) Ripple of DC voltages. (c) Powers of module 1 to module 3.

$E_1 = E_4 = 1000$ W/m^2, $E_2 = E_3 = 900$ W/m^2, $P_1 = P_4 = 229$ W, and $P_2 = P_3 = 206$ W). When the irradiation level of panel 2 drops from 900 to 200 W/m^2, the system switches from mode 1 to mode 2, realizing smooth transition. On the basis of mode 2, when the irradiation level of panel 3 drops from 900 to 600 W/m^2, the system switches from mode 2 to mode 3, as shown in Fig. 14(b). The steady-state waveforms of the three modes are shown in Fig. 14(c)–(k). The grid-connected current THD of the three modes is 1.2%, 1.8%, and 2.2%, respectively. It can be seen that the ORPCS proposed in this article achieves a high-quality grid-connected current.

The comparison between ORPCS, RPCS, HCS, and THCS is shown in Figs. 15 –18. The comparison conditions are: $E_1 = E_2 = 1000$ W/m^2, $E_3 = E_4 = 100$ W/m^2, $P_1 = P_2 = 229$ W, $P_3 = P_4 = 20$ W, and the temperature is 45°. Under this condition, the imbalance of power between different panels is large, which exceeds the range of the unity PF operation. If no reactive power is injected, ORPCS, RPCS, HCS, and THCS cannot harvest all energies from each panel. On the contrary, injecting reactive power can achieve more energy harvested.

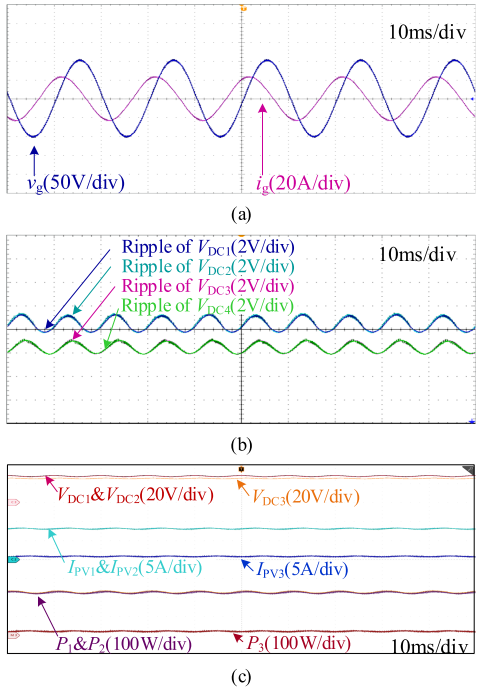

Fig. 16. Experimental waveforms of RPCS. (a) AC voltage and current. (b) Ripple of DC voltages. (c) Powers of module 1 to module 3.

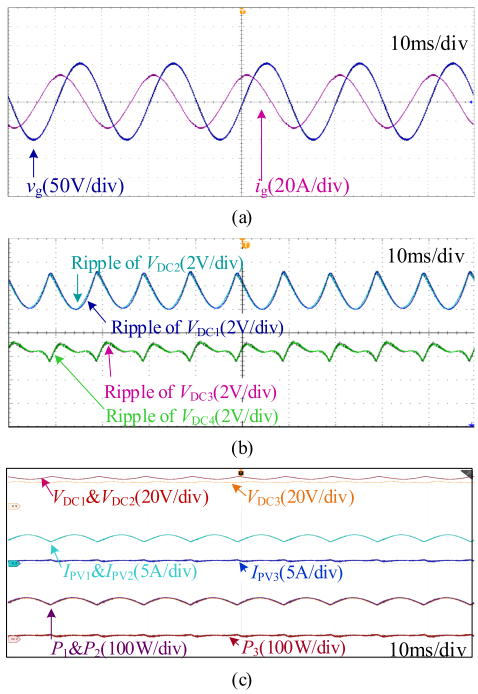

Fig. 17. Experimental waveforms of HCS. (a) AC voltage and current. (b) Ripple of DC voltages. (c) Powers of module 1 to module 3.

Fig. 15 shows the waveform of the ORPCS. The reactive current is 7 A rms, the output voltage of panel 1 fluctuates with $\Delta u = 0.78$ V, and the power harvested by the system at the PCC is 479 W. However, the reactive current of RPCS (see Fig. 16) is 15.3 A rms. The excessive reactive current and dc voltage

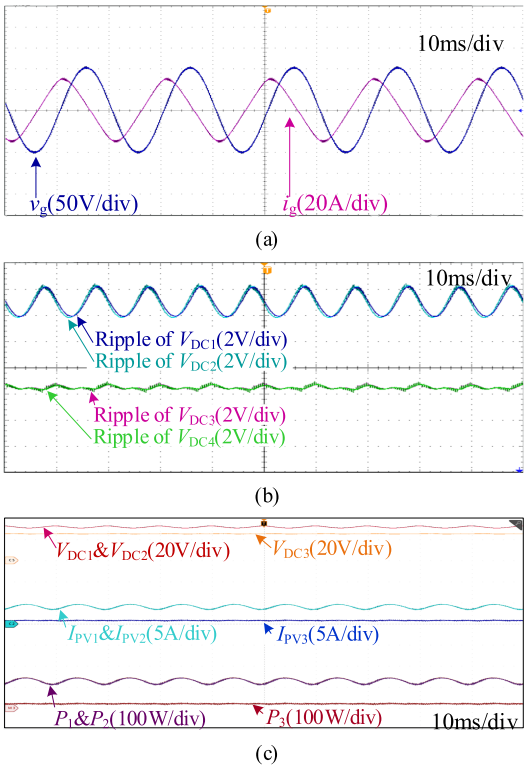

Fig. 18. Experimental waveforms of THCS. (a) AC voltage and current. (b) Ripple of DC voltages. (c) Powers of module 1 to module 3.

TABLE IV
POWER HARVESTED AT PCC

Strategy	THCS	HCS	RPCS	ORPCS
Power(W)	316	380	448	479

fluctuation ($\Delta u = 1.42$ V) cause RPCS to harvest only 448 W at PCC (31 W less than ORPCS).

The maximum grid-connected current that the experimental platform can output is 30 A peak (21.2 A rms). If it exceeds 30 A, it will run in current-limiting mode to prevent overcurrent. The peak grid-connected current of ORPCS and RPCS is 13.7 A and 23.5 A, respectively, which do not exceed the upper limit and the MPPT of each panel can be achieved.

It can be seen from the simulation that the reactive power requirements of HCS and THCS are too much, which exceeds the upper limit of system, so they work in current-limiting mode, as shown in Figs. 17 and 18. As a result, HCS and THCS cannot achieve the MPPT of the higher power panels and cannot realize the full harvest of PV output energy, which will lead to more energy loss.

The harvested power at the PCC measured by the high-performance power analyzer YOKOGAWA WT1800 is shown in Table IV. It can be seen that the ORPCS proposed in this article harvests the most PV energies with the least reactive power under severe imbalance compared with THCS, HCS, and RPCS.

Fig. 19 checks the system performance under a polluted grid. The grid contains 10% of the third harmonic. When the resonant control signal is not added to the modulation signal of each HB, the grid-connected current THD = 26%, as shown in Fig. 19(a).

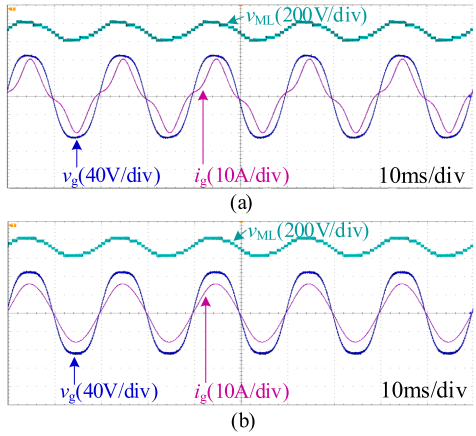

Fig. 19. Experimental waveforms under polluted grid. (a) Without resonant controller. (b) With resonant controller.

After adding the resonant control signal, as shown in Fig. 10, to the modulation signals of each HB, the grid-connected current waveform is shown in Fig. 19(b), with the grid-connected current THD = 2.26%.

VI. CONCLUSION

The novelty of this article is that it proposes an optimized strategy based on HCS and RPCS to achieve minimal reactive power injection while retaining all the advantages of HCS. ORPCS can achieve more energy harvesting in severe unbalanced conditions.

1) This article first analyzes the reasons why the existing methods THCS, HCS, and RPCS cannot achieve the minimum reactive power operation under the condition of severe unbalanced PV output powers. Then, the reason why the combination of HCS and RPCS, HCS–RPCS, also cannot achieve the minimum reactive power operation is analyzed.
2) Then, this article proposes a strategy. When the MI of a module reaches 1.27, this strategy enables this module, which realize that the fundamental component of the output voltage and the ac current is in the same phase. This is the basis for achieving minimum reactive power operation.
3) When the highest MI is greater than 1.27, this article proposes a strategy to make the system operate in the linear modulation region, achieve the minimum reactive operation, and harvest more PV energy.

REFERENCES

[1] J. Rodriguez, S. Bernet, B. Wu, J. O. Pontt, and S. Kouro, "Multilevel voltage-source-converter topologies for industrial medium-voltage drives," *IEEE Trans. Ind. Electron.*, vol. 54, no. 6, pp. 2930–2945, Dec. 2007.
[2] J.-S. Lai and F. Z. Peng, "Multilevel converters—A new breed of power converters," *IEEE Trans. Ind. Appl.*, vol. 32, no. 3, pp. 509–517, May/Jun. 1996.
[3] M. Marchesoni, M. Mazzucchelli, and S. Tenconi, "A non conventional power converter for plasma stabilization," in *Proc. IEEE 19th Annu. Power Electron. Specialists Conf.*, Kyoto, Japan, 1988, vol. 1, pp. 122–129.

[4] E. Babaei, S. Laali, and S. Alilu, "Cascaded multilevel inverter with series connection of novel H-bridge basic units," *IEEE Trans. Ind. Electron.*, vol. 61, no. 12, pp. 6664–6671, Dec. 2014.
[5] Y. Zhang, X. Chen, and J. Sun, "Sequence impedance modeling and analysis of MMC in single-star configuration," *IEEE Trans. Power Electron.*, vol. 35, no. 1, pp. 334–346, Jan. 2020.
[6] J. Chavarria, D. Biel, F. Guinjoan, C. Meza, and J. J. Negroni, "Energy-balance control of PV cascaded multilevel grid-connected inverters under level-shifted and phase-shifted PWMs," *IEEE Trans. Ind. Electron.*, vol. 60, no. 1, pp. 98–111, Jan. 2013.
[7] Z. Zhang, H. Zhao, S. Fu, J. Shi, and X. He, "Voltage and power balance control strategy for three-phase modular cascaded solid stated transformer," in *Proc. IEEE Appl. Power Electron. Conf. Expo.*, Long Beach, CA, USA, 2016, pp. 1475–1480.
[8] Y. Yu, G. Konstantinou, B. Hredzak, and V. G. Agelidis, "Operation of cascaded H-bridge multilevel converters for large-scale photovoltaic power plants under bridge failures," *IEEE Trans. Ind. Electron.*, vol. 62, no. 11, pp. 7228–7236, Nov. 2015.
[9] E. Villanueva, P. Correa, J. Rodriguez, and M. Pacas, "Control of a single-phase cascaded H-bridge multilevel inverter for grid-connected photovoltaic systems," *IEEE Trans. Ind. Electron.*, vol. 56, no. 11, pp. 4399–4406, Nov. 2009.
[10] C. Cecati, F. Ciancetta, and P. Siano, "A multilevel inverter for photovoltaic systems with fuzzy logic control," *IEEE Trans. Ind. Electron.*, vol. 57, no. 12, pp. 4115–4125, Dec. 2010.
[11] T. Zhao et al., "An optimized third harmonic compensation strategy for single-phase cascaded H-bridge photovoltaic inverter," *IEEE Trans. Ind. Electron.*, vol. 65, no. 11, pp. 8635–8645, Nov. 2018.
[12] M. A. Rezaei, S. Farhangi, and H. Iman-Eini, "Extending the operating range of cascaded H-bridge based multilevel rectifier under unbalanced load conditions," in *Proc. IEEE Int. Conf. Power Energy*, 2010, pp. 780–785.
[13] A. Eskandari, V. Javadian, H. Iman-Eini, and M. Yadollahi, "Stable operation of grid connected cascaded H-bridge inverter under unbalanced insolation conditions," in *Proc. IEEE 3rd Int. Conf. Electr. Power Energy Convers. Syst.*, 2013, pp. 1–6.
[14] H. Iman-Eini, S. Bacha, and D. Frey, "Improved control algorithm for grid-connected cascaded H-bridge photovoltaic inverters under asymmetric operating conditions," *IET Power Electron.*, vol. 11, no. 3, pp. 407–415, Mar. 2018.
[15] Y. Ko, M. Andresen, G. Buticchi, and M. Liserre, "Power routing for cascaded H-bridge converters," *IEEE Trans. Power Electron.*, vol. 32, no. 12, pp. 9435–9446, Dec. 2017.
[16] T. Zhao, X. Zhang, W. Mao, F. Wang, J. Xu, and Y. Gu, "A modified hybrid modulation strategy for suppressing DC voltage fluctuation of cascaded H-bridge photovoltaic inverter," *IEEE Trans. Ind. Electron.*, vol. 65, no. 5, pp. 3932–3941, May 2018.
[17] M. Miranbeigi and H. Iman-Eini, "Hybrid modulation technique for grid-connected cascaded photovoltaic systems," *IEEE Trans. Ind. Electron.*, vol. 63, no. 12, pp. 7843–7853, Dec. 2016.
[18] M. Moosavi, G. Farivar, H. Iman-Eini, and S. M. Shekarabi, "A voltage balancing strategy with extended operating region for cascaded H-bridge converters," *IEEE Trans. Power Electron.*, vol. 29, no. 9, pp. 5044–5053, Sep. 2014.
[19] M. Wang et al., "Harmonic compensation strategy for single-phase cascaded H-bridge PV inverter under unbalanced power conditions," *IEEE Trans. Ind. Electron.*, vol. 67, no. 12, pp. 10474–10484, Dec. 2020.
[20] T. Zhao et al., "Harmonic compensation strategy for extending the operating range of cascaded H-bridge PV inverter," *IEEE J. Emerg. Sel. Topics Power Electron.*, vol. 8, no. 2, pp. 1341–1350, Jun. 2020.
[21] T. Zhao and D. Chen, "A power adaptive control strategy for further extending the operation range of single-phase cascaded H-bridge multilevel PV inverter," *IEEE Trans. Ind. Electron.*, vol. 69, no. 2, pp. 1509–1520, Feb. 2022.
[22] C. Wang, M. Chen, and Y. Jie, "A reactive power control optimization scheme for the power imbalance of cascaded photovoltaic converter," in *Proc. IEEE Energy Convers. Congr. Expo.*, 2021, pp. 123–129.
[23] L. Liu, H. Li, Y. Xue, and W. Liu, "Decoupled active and reactive power control for large-scale grid-connected photovoltaic systems using cascaded modular multilevel converters," *IEEE Trans. Power Electron.*, vol. 30, no. 1, pp. 176–187, Jan. 2015.
[24] N. D. Marks, T. J. Summers, and R. E. Betz, "Reactive power requirements for cascaded H-bridge photovoltaic systems," in *Proc. IEEE 40th Annu. Conf. Ind. Electron. Soc.*, 2014, pp. 2219–2225.
[25] M.-A. Rezaei, H. Iman-Eini, and S. Farhangi, "Grid-connected photovoltaic system based on a cascaded H-bridge inverter," *J. Power Electron.*, vol. 12, no. 4, pp. 578–586, Jul. 2012.
[26] Y. Zhou and H. Li, "Analysis and suppression of leakage current in cascaded-multilevel-inverter-based PV systems," *IEEE Trans. Power Electron.*, vol. 29, no. 10, pp. 5265–5277, Oct. 2014.
[27] V. V. S. Pradeep Kumar and B. G. Fernandes, "Minimization of inter-module leakage current in cascaded H-bridge multilevel inverters for grid connected solar PV applications," in *Proc. IEEE Appl. Power Electron. Conf. Expo.*, 2016, pp. 2673–2678.
[28] Y. Zhou and H. Li, "Leakage current suppression for PV cascaded multilevel inverter using GaN devices," in *Proc. IEEE Energy Convers. Congr. Expo.*, 2013, pp. 1304–1310.
[29] X. She, A. Q. Huang, T. Zhao, and G. Wang, "Coupling effect reduction of a voltage-balancing controller in single-phase cascaded multilevel converters," *IEEE Trans. Power Electron.*, vol. 27, no. 8, pp. 3530–3543, Aug. 2012.
[30] A. G. Yepes, F. D. Freijedo, J. Doval-Gandoy, Ó. López, J. Malvar, and P. Fernandez-Comesaña, "Effects of discretization methods on the performance of resonant controllers," *IEEE Trans. Power Electron.*, vol. 25, no. 7, pp. 1692–1712, Jul. 2010.

Jinyu Li (Graduate Student Member, IEEE) was born in Jiangsu, China, in 1989. He received the B.S. degree from Huaiyin Normal University, Huaian, China, the M.S. degree from the Anhui University of Technology, Maanshan, China, in 2012 and 2015, respectively, both in electrical engineering. He is currently working toward the Ph.D. degree in electrical engineering with the Nanjing University of Aeronautics and Astronautics, Nanjing, China.

His main research interests include the modeling, design and control of multilevel converters, renewable energy generation systems, and power system of more electric aircraft.

Jie Chen (Member, IEEE) received the B.S. and Ph.D. degrees in electrical engineering from the Nanjing University of Aeronautics and Astronautics (NUAA), Nanjing, China, in 2004 and 2011, respectively.

In October 2011, he joined as a Lecturer with the College of Automation Engineering, NUAA, where he is currently an Associate Professor. From November 2018 to November 2019, he was a visiting faculty with the Center for Ultra-Wide-Area Resilient Electric Energy Transmission Networks, Department of Electrical Engineering and Computer Science, University of Tennessee, Knoxville, TN, USA. His research interests include the modeling, design and control of power electronic converters or systems, renewable energy generation systems, and power system of more electric aircraft.

Chunying Gong (Member, IEEE) was born in Zhejiang, China, in 1965. She received the B.S., M.S., and Ph.D. degrees in electrical engineering from the Nanjing University of Aeronautics and Astronautics (NUAA), Nanjing, China, in 1984, 1990, and 1993, respectively.

From 1984 to 1987, she was an Electrical Assistant Engineer with Chengdu Aircraft Design and Research Institute. In 1993, she joined as a Lecturer with the College of Automation Engineering, NUAA, where she became an Associate Professor and a Professor, in 1996 and 2004, respectively. In 2009, she was a Senior Research Fellow with the Department of Electrical, Computer, and Systems Engineering, Rensselaer Polytechnic Institute, New York, NY, USA. Her research focuses on power electronic systems design and control, renewable energy, and distributed generation.